3.2 Tests by Monte-Carlo Methods

The outcome of the pattern recognition methods and event reconstruction procedures depends heavily on the accuracy of the software carrying out the tasks discussed in the previous sections. The reliability of the software was tested by simulating the positions of the tracks for known kinematic conditions, in all the detection planes of the experimental apparatus, and by reconstructing them with the same code used for the real data. The actual experimental situations are represented as closely as possible by the simulation code. The measured uncertainties of the detectors and the effects that arise from multiple scattering in air and other materials (including the target and the material used in constructing various detectors) in the path of the tracks smear the track locations at each detector plane.

The excitation energy of the projectile for the 1p+^{27}Al and the 1n+^{27}Si decay channels were incorporated by convoluting the excitation energy observed in photo-absorption studies taken from the references [12, 13, 14], with the corresponding virtual photon spectrum. For other decay channels, the excitation energy distributions of Gaussian forms were used since the detailed comparison of low energy data with full event reconstructions were made for only these two channels in this thesis. In addition, to study the 1n+^{27}Si channel, the response of the neutron calorimeter energy distribution was built into the simulation since the energy measurements of the neutron calorimeters play an essential role for this channel.

The simulation also enables the study of the contributions from the various factors that affect the resolution of the reconstructed quantities. These arise from the position distortions caused by the detector resolution and by multiple scattering which is not accounted for by the optimum track fitting method. The real uncertainty in the recontruction was obtained by performing tests with the simulation of various reconstructed parameters. The results of these studies for 1p+^{27}Al and 1n+^{27}Si are shown in Tables 5.3 and 5.4 respectively.

Table 5.3: Reconstruction resolution for 1p events.

Source of Uncertainty ^{28}Si→1p+^{27}Al	σ_M (MeV)	σ_{θ^*} (Degrees)	σ_{ϕ^*} (Degrees)
Detector resolution	0.5	1.0	2.5
Multiple scattering with no target	0.2	0.5	0.8
Total for Al target	0.6	1.3	3.2
Total for Cu target	0.7	1.6	4.0
Total for Sn target	1.0	2.1	5.0
Total for Pb target	1.1	2.6	6.0

An estimate of the systematic errors in the final state energy scale that arise from the uncertainty in the beam momentum, the field strength and the effective length

Table 5.4: Reconstruction resolution for 1n events.

Source of Uncertainty ^{28}Si$\rightarrow$1n+^{27}Si	σ_M (MeV)	σ_{θ^*} (Degrees)	σ_{ϕ^*} (Degrees)
Detector resolution	1.5	19.5	3.9
Multiple scattering with no target	1.1	7.6	0.3
Total for Al target	2.2	24.6	3.9
Total for Cu target	2.0	27.9	4.0
Total for Sn target	1.9	27.7	4.1
Total for Pb target	1.9	28.0	4.2

of the spectrometer magnets, and the detector alignments, is also obtained from the simulation code. The estimated systematic error was less that 0.5 MeV.

CHAPTER 6

Analysis of Complex Channels

The results of the analysis of the peripheral data are described here. We have evaluated cross sections for a number of peripheral channels including those with α and d in the final state. In addition, we have measured excitation energy distributions for 1p+^{27}Al and 1n+^{27}Si through kinematic reconstruction. The possibilities of multi photon excitations and the effect on electromagnetic excitations by soft nuclear interactions are also investigated.

A Cross Section Measurements

In chapter 4, a discussion of the method used to extract cross sections for two of the simplest channels was given. The cross section analysis for exclusive channels with several nucleons in the final state is difficult if we require identification of each final state particle. Although the heavy ion charge selection through a triple charge measurement works very well for these channels, the efficiency of track reconstruction decreases with increasing multiplicity and the assignment of energy to overlapping hits in the calorimeter is very difficult. We therefore searched for a superior method to identify the channels.

1 P/Z by Drift Chambers

The P/Z of the heavy fragment will change by roughly 4% for the removal of each nucleon. The studies with drift chambers showed that the heavy fragment P/Z can be reconstructed with ~1% resolution. Since we can select a heavy ion charge with 2% resolution, this extra measurement helps to overcome the difficulties in identifying different isotopes.

Figure 6.1 (a) shows the measured magnetic rigidity (P/Z) for the heavy ion fragments with selected Z=13. The well resolved peaks in the plot correspond to different isotopes. They are 1p+^{27}Al, 1p+1n+^{26}Al and 1p+2n+^{25}Al. Figure 6.1 (b) shows the measured charge versus P/Z for heavy ion fragments. Each cluster of hits corresponds to a different peripheral channel. It should be mentioned here that we require the aid of calorimeters and other available detectors to separate the channels with a heavy ion of same P/Z but with different final states (such as 3p+2n+^{23}Na and 1p+1α+^{23}Na). But for most of the channels we only need to apply very loose cuts in the energy measurements of the calorimeters.

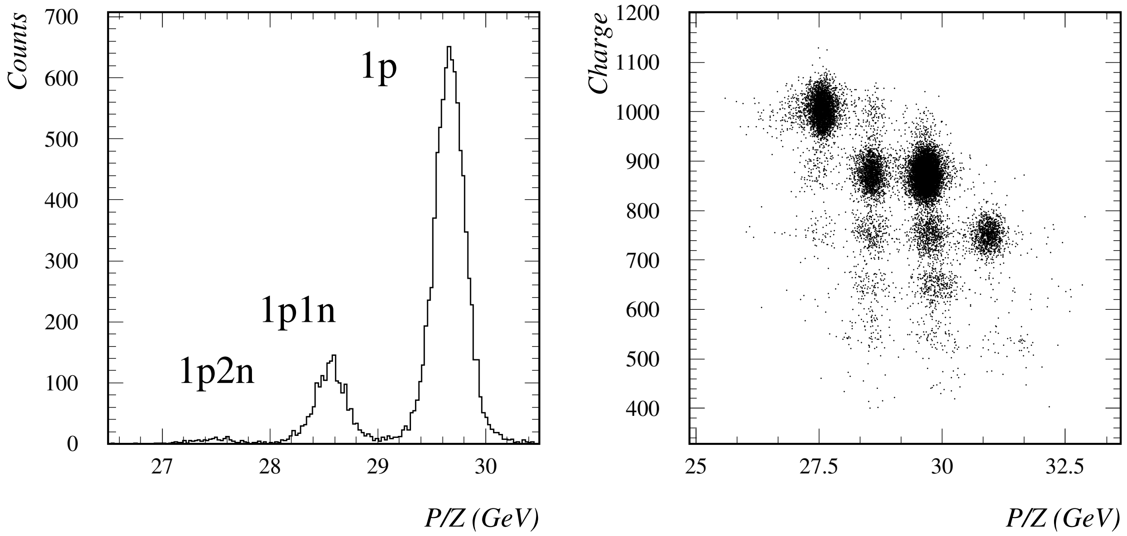

Figure 6.1: P/Z reconstruction. (a) Selected Z=13 events. (b) Charge vs. P/Z for different decay channels.

The major inefficiency for heavy ion track reconstruction arises from the beam vertex detector measurements. One plane of the beam vertex fails to report the hit location of the passing beam tracks for roughly 10-15% of the events. Therefore it is not possible to calculate the incoming beam angle for these events. However, it was found that the beam converging point was more or less concentrated in an $\sim$1mm diameter area, the center of which varied for different runs due to beam tuning. A running average of the beam converging point was calculated on an event by event basis. This location and the location reported by the working plane were used to reconstruct the tracks for the events in which one plane of the beam vertex failed to report the beam location. A χ^2 cut was applied to all the reconstructed tracks to reject the bad reconstructions caused by problems in the drift chambers.

2 Event Classification

2.1 Selection Procedure

We consider now the identification of specific channels using the P/Z measurement described above. Let us consider the selection of the 3p channel. The Z=11 candidates were first selected by the triple charge measurement. Figure 6.2 (a) shows the neutron calorimeter energy verses the reconstructed P/Z for Z=11 candidates. The isotopes such as 3p+^{25}Na, 3p+1n+^{24}Na and 3p+2n+^{23}Na which belong to the 3p group can easily be identified. Among the other groups we can identify possible candidates for 2p+1d+^{24}Na and 1p+1α+^{23}Na, which need further classification. Figure 6.2 (b) shows the energy in proton calorimeters for selected Z=11 candidates (solid curve). It is impossible to decide where to put the cut on this spectrum to select 3 proton events. Note that although we require Z=11 for heavy ions, the channels with α or d in the final state will have only 1 or 2 protons deflecting into the proton calorimeters. The dashed line shows the 3p+Xn+^{Y}Na (where X=0-2 and Y=25-23) candidates selected by combining the P/Z and the neutron calorimeter energy for Z=11 candidates (ie, by requiring the correct neutron energy and the heavy ion P/Z for each isotope). This shows how clean channels can be selected even without the energy measurement in the proton calorimeters.

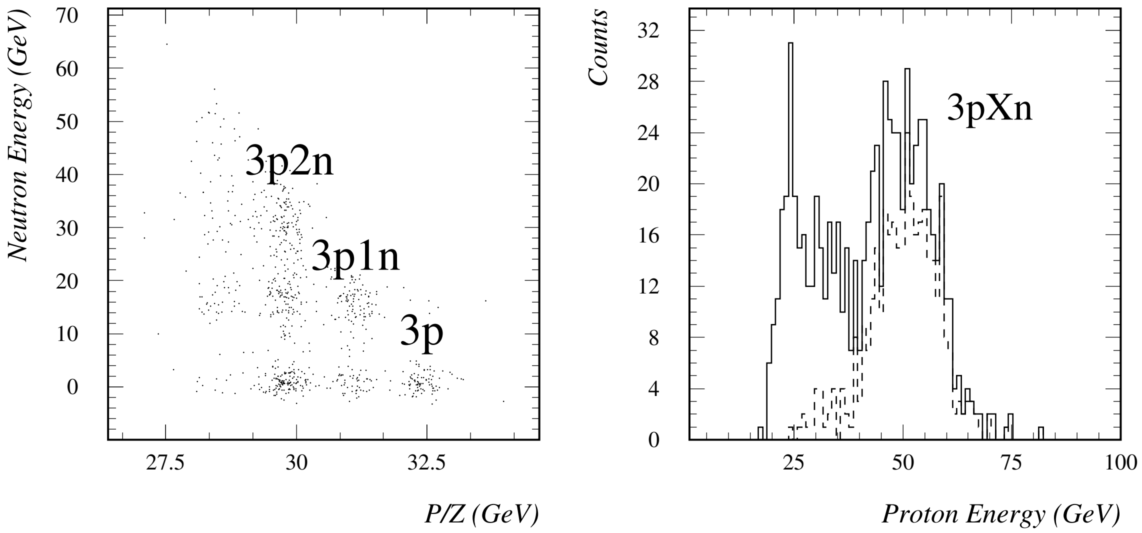

Figure 6.2: Selection of multi nucleon events. (a) Energy in neutron calorimeters vs. P/Z. (b) Energy in proton calorimeters for selected Z=11 events (solid curve) and selected Z=11 with cuts on neutron energy and the P/Z (dashed curve).

2.2 Selection of α and d Channels

The channels having α or d in the final state require an additional measurement to indicate their presence. The P/Z of these particles is very close to the P/Z of the heavy fragments accompanying them. In drift chambers, these particles traverse in the reduced gain region which is suitable for heavy ion fragments and only a very small percentage will leave recognizable tracks in the drift section as well as in the pad section. Hence, efficient track reconstruction is not possible for these particles.

A closer inspection shows that the vertical and the horizontal hodoscopes at the downstream end of the spectrometer can help us resolve this problem. The pattern recognition algorithm was developed to search for the second highest pulse height in either the vertical or the horizontal scintillation counters (after selecting the heavy ion fragment). Since the counters are perpendicular to each other, we can narrow the region in which the heavy ion and the secondary particle (α or d) overlap to an area of about 10x10 cm^2. Figures 6.3 (a) and (b) show the measured second maximum pulse height for selected 1p+1d+^{23}Mg and 1p+1α+^{23}Na events. The second highest pulse height shows that particles with Z=1 and Z=2 (in this plot they are at 100 and 400) have traversed the scintillators, which indicates the presence of d and α. The cuts were applied on these distributions at 50 and 250 (only to reject low pulse heights), to select the d and α channels respectively.

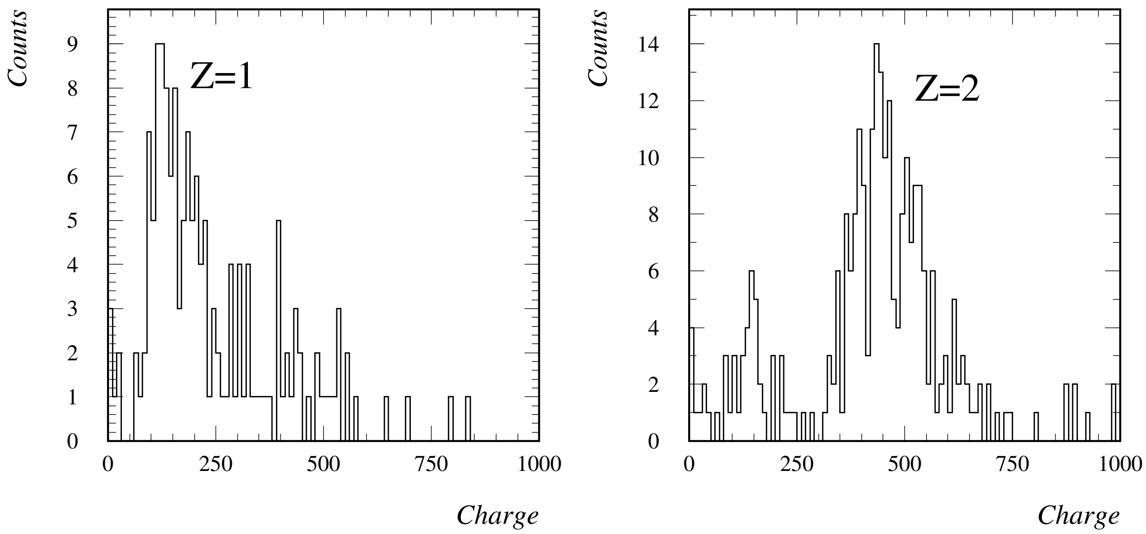

Figure 6.3: Second charge measurement at the downstream end of the spectrometer. (a) d channels. (b) α channels.

In order to confirm our identification of the complex final states, we look for collaborating evidence in the downstream calorimeters. Studies showed that for the selected events with d and α channels, the deflected beam region calorimeters on an average report an energy measurement higher than what we expect from the residual heavy ion. This indicated the presence of another particle in the same vicinity as the heavy ion fragment confirming our selection procedure. No requirements on the energy measurement was imposed due to the poor energy resolution in the deflected beam region calorimeters. However, one should bear in mind that the heavy ion usually creates δ rays which can be misidentified as the correct second highest pulse height in the forward scintillators. Hence the selection on d and α channels can be somewhat biased.

3 Results

3.1 Efficiencies

In addition to the efficiencies listed in Table 4.6, the major inefficiency for this analysis arises from the heavy ion reconstruction. This can be estimated for simple channels by selecting 1p+^{27}Al or 1n+^{27}Si with and without using the P/Z measurement since these are very clean channels which can be analyzed without the P/Z measurement. For rare channels, 2p+^{26}Mg was used as the reference channel. It was found that the P/Z efficiency is almost the same for all the heavy ion fragments.

All α and d channels suffer due to the limited acceptance in the detectors. This inefficiency was estimated by using Monte-Carlo methods to simulate the decay of specific channels and by then estimating the number of events that fall outside the 10x10 cm^2 area. This estimation obviously depends on the available excitation energy for the decay since the opening angle between the heavy ion and the α or d depends on this energy. Figures 6.4 (a) and (b) show the estimated efficiency for 1p+1d+^{25}Mg and 1p+1α+^{23}Na against the excitation energy used (open circles). An efficiency of 70% was used in this analysis for the acceptance corrections of all channels having α or d emissions.

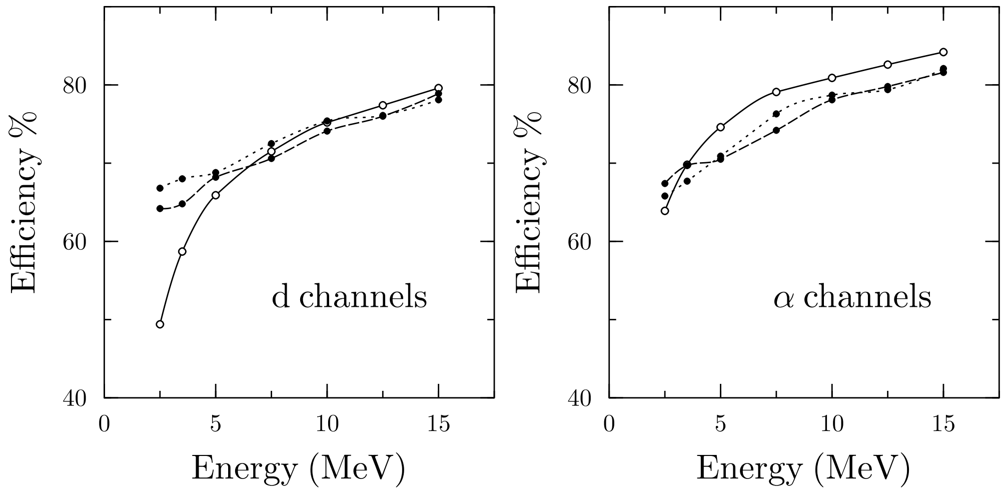

Figure 6.4: Efficiency of limited acceptance arising from the second charge measurement. Plots show the estimated efficiency variations for excitation energies up to 20 MeV. Each curve represents a specific decay channel having (a) *d* and (b) α particle in the final state.

The other efficiency factors arise from the performance of the calorimeters in detecting multinucleon events (which can be obtained by folding the efficiency to detect a single nucleon) and the trigger efficiencies for 2n and 3p triggers [1] due to the assigned thresholds. No acceptance corrections were needed for detecting peripheral protons or neutrons since the low P_T generated in the electromagnetic interactions does not deflect nucleons out of our detector acceptance limits. A list of estimated efficiencies is given in Table 6.1.

[1]The efficiency for the 2p trigger threshold is 100%

Table 6.1: Estimated efficiencies for selection of multi nucleon events.

Selection	Efficiency %
2n triggers	52.0 ±10.0
3p triggers	72.0 ± 5.0
P/Z reconstruction	85.2 ± 2.5

3.2 Cross Sections

The cross section calculations were carried out for each identified channel using the equation 4.1 given in chapter 4. The results for channels having neutrons and protons in the final state are given in Table 6.2 and the results for the channels with an α or a d in the final state are given in Table 6.3. These data are corrected for interactions outside of the target by subtracting the appropriately scaled rates of events observed with the empty target frame. The listed errors are only statistical.

Table 6.2: Measured exclusive EMD cross sections for channels having neutrons and protons in the final state. The listed errors are only statistical.

Channel	Pb (mb)	Sn (mb)	Cu (mb)	Al (mb)
1p	676.42±7.63	274.04±4.35	111.03±3.30	31.55±1.19
1n	241.03±4.18	100.01±2.00	40.42±1.67	13.11±0.59
1p1n	65.05±2.47	27.50±1.43	10.18±1.09	4.04±0.43
2p	74.69±0.80	34.36±0.47	13.09±0.24	4.32±0.12
2p1n	22.76±0.44	10.47±0.26	4.69±0.15	1.99±0.08
2p2n	5.95±0.23	2.95±0.14	1.54±0.08	0.66±0.04
2n	1.90±0.11	0.74±0.07	0.27±0.04	0.12±0.02
2n1p	3.45±0.15	1.64±0.09	0.76±0.05	0.34±0.03
3p	0.57±0.05	0.16±0.02	0.07±0.01	0.04±0.01
3p1n	0.82±0.06	0.39±0.03	0.15±0.02	0.10±0.01
3p2n	1.21±0.07	0.58±0.04	0.25±0.02	0.13±0.01
4p	0.011±0.006	0.002±0.002	–	–
4p1n	0.016±0.008	0.006±0.005	0.004±0.003	0.003±0.002
4p2n	0.109±0.018	0.053±0.011	0.025±0.006	0.015±0.004
4p3n	0.073±0.015	0.050±0.011	0.037±0.008	0.007±0.003

In Figure 6.5 (a), the measured EMD cross sections are displayed as functions of the Q_0 of the decay channel (open circles). The general trend of the data shows an exponential decrease with the increase in the value of Q. A difference is observed in the cross sections of the xp and yn channels. This is evident by the 2p and 2n cross sections given in the Table 6.2. The decay modes of the excited ^{28}Si nucleus in the

Table 6.3: Measured exclusive EMD cross sections for channels having d and α in the final state (in addition to the neutrons and protons). Listed errors are only statistical.

Channel	Pb (mb)	Sn (mb)	Cu (mb)	Al (mb)
1α	72±32	58±30	17±19	21±16
1p1α	24.69±1.74	10.16±1.00	5.83±0.90	2.00±0.36
1n1α	3.41±0.60	1.60±0.30	0.24±0.16	0.16±0.07
1p1n1α	7.37±1.00	1.97±0.46	1.63±0.51	0.71±0.22
2p1α	2.30±0.15	1.23±0.09	0.47±0.05	0.26±0.03
2p1n1α	2.61±0.15	1.14±0.09	0.66±0.06	0.27±0.03
2p2n1α	1.13±0.10	0.63±0.07	0.25±0.03	0.11±0.02
1p1d	20.07±1.57	8.56±0.91	4.14±0.76	1.39±0.30
1n1d	6.60±0.83	2.24±0.36	1.43±0.37	0.14±0.07
1p1n1d	5.40±0.86	3.05±0.57	2.73±0.65	0.95±0.25
2p1d	2.94±0.34	1.45±0.19	0.95±0.13	0.33±0.07
2p1n1d	3.12±0.35	1.76±0.21	0.93±0.13	0.28±0.06
2p2n1d	0.53±0.10	0.21±0.05	0.18±0.04	0.08±0.02

GDR region are discussed elsewhere [12, 13], where both statistical and non statistical decays are found. Assuming a purely statistical decay, calculations were performed to understand the general trend [19]. For these calculations, known photo-absorption cross sections were folded with virtual photon spectrums to obtain the excitation energy, and the simulation code CASCADE [21] was used to follow the subsequent decay of ^{28}Si. These results are shown in figure 6 (closed circles). The calculations show good agreement with the measured data. However, this comparison shows that in general, these calculations overpredict the proton emission cross sections and underpredict the neutron emission channels. In addition, the α emission channels which are purely statistical [12] decay channels show cross sections well below the calculated values.

The charge-changing cross sections previously measured at AGS energies [23] are shown in figure 6.5 (b) (closed circles). These cross sections define an upper limit to the cross sections we measure. Our measured cross sections which are shown in the same plot (open circles), agree well for all but ΔZ=4 which is expected since our exclusive cross sections do not contain all the decay channels. Here the α and d channels are also included in calculating semi-inclusive cross sections. No data were available in the above reference to compare with the 1n emission cross section.

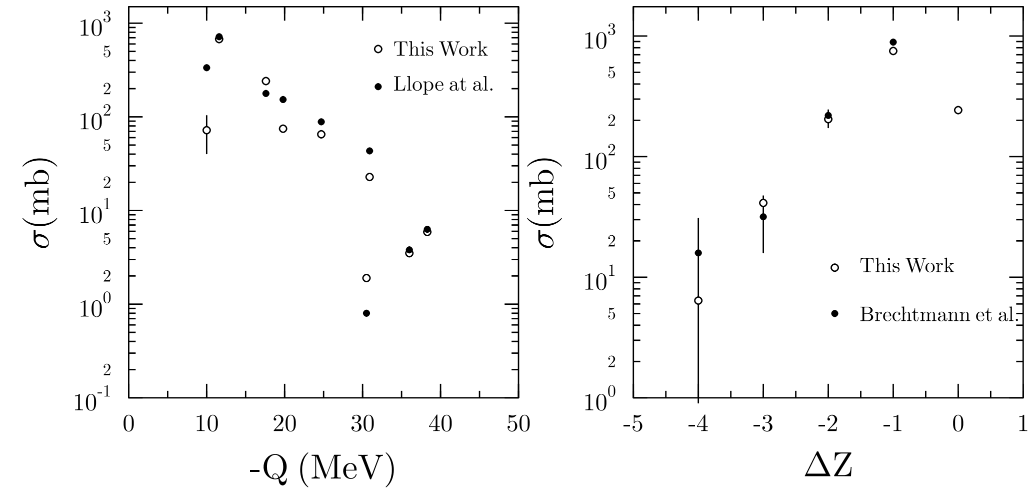

Figure 6.5: (a) Exclusive cross section vs. Q value of the reaction. (b) Total charge changing cross sections.

B Interpretation of the Data

1 Z and A Dependence

The production cross section was investigated as a function of the target, and this was used to characterize the nature of the reaction mechanism. The principal background to the EMD process is due to the soft nuclear induced fragmentation. The probability for these collisions is dependent on the target size while the probability for the EMD depends on the target charge. The measured single proton emission cross section as a function of the target charge for five different targets is shown in Figure 6.6. These cross sections show a strong charge dependence but do not show a simple Z_T scaling. A fit was performed on the data to obtain the dependence of the EMD cross sections on Z_T, assuming the following dependence of the cross section.

$$\sigma = a({A_T}^{1/3} + {A_P}^{1/3}) + bZ_T^c \tag{6.1}$$

In the above equation, a, b and c are considered as three free parameters, and, A_T, A_P and Z_T represent the target mass, the projectile mass and the target charge respectively. The first term scales as the sum of the radii of the target and projectile mass. This is expected to describe the target dependence of the nuclear component. The second term scales as a power of the target charge and is expected to describe the target dependence of the electromagnetic component. The values of the parameters obtained from the fit are; $a = 1.39 \pm 0.20$, $b = 0.23 \pm 0.05$ and $c = 1.80 \pm 0.06$. Figure 6.6 shows the contribution of each term to the cross section. A non negligible contribution from the nuclear process for low Z targets is indicated by the results. However, due to severe biases introduced by the trigger and the analysis, the value obtained for a by this fit cannot be taken as a measurement of the nulear component of the cross section. The observed $Z^{1.8}$ dependence of the electromagnetic component agrees well with the values obtained in other EMD studies [18]. Although for low Z targets the nuclear component is substantial, the background to EMD for high Z targets is negligible. This opens up the possibility of meaningful detailed studies using kinematic reconstruction.

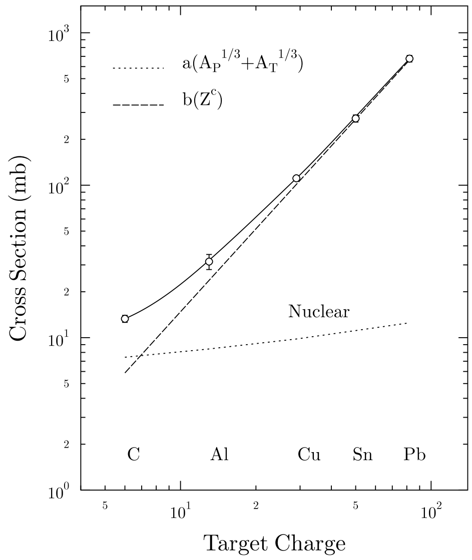

Figure 6.6: Z and A dependence of EMD cross sections for the ^{28}Si $\rightarrow$ ^{27}Al + 1p reaction. Solid curve represents the 3 parameter fit discussed in the text. Contributions of the extracted electromagnetic (dashed) and nuclear (dotted) components are also shown.

So far in this discussion, we have concentrated on the electromagnetic interactions which we claim do not produce any activity in the target region. In order to confirm our suspicion that events showing activities in the target region are indeed nuclear events, we examine whether they show the expected dependence on the target mass A_T. Two event samples were extracted from pre-selected nuclear events for the reactions 1p+1n+^{26}Al and 2p+1n+^{25}Mg by selecting P/Z and the charge Z of the heavy fragments. The events which show a correct number of protons but no neutrons (in this case a missing neutron) at the downstream end of the spectrometer were then selected. Figure 6.7 (a) shows the energy in the participant calorimeter for 1p+1n+^{26}Al events. This plot shows that the missing neutron at the downstream end has deflected into the participant calorimeter. The events with an energy of 2.5 GeV or above in the participant calorimeter were selected as a good sample for nuclear interactions. Figure 6.7 (b) shows the cross section dependence on the mass of the target for these selected nuclear events. The dashed lines are the best fit to the data with the dependence of $a(A_T{}^k + A_P{}^k)$ with a and k considered as free parameters. The value of k which is expected to be 0.33 was found to be 0.39$\pm$0.07 for the 1p1n channel and 0.46$\pm$0.08 for the 2p1n channel. Note that we cannot consider the given cross sections in Figure 6.7 as absolute nuclear cross sections since the selected samples were triggered to select electromagnetic interactions at the trigger level. However, it is clear from this plot that nuclear events do show a strong target mass dependence.

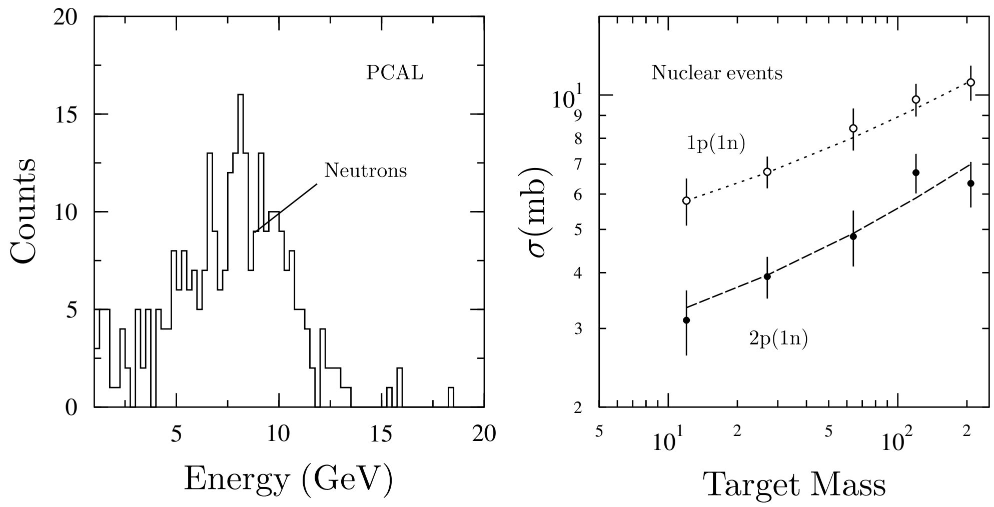

Figure 6.7: Selected nuclear events. (a) Measured energy in PCAL for missing neutrons. (b) Estimated cross sections. Dashed and dotted lines represent the expected behavior for a pure nuclear dependence.

2 Double Photon Excitations

In peripheral collision studies, one of the major goals is to see if we can identify the multi photon processes where the projectile absorbs two or more virtual photons from the same target nuclei [63, 64]. The simplest approach to this is to see if we observe any deviations from the $Z^{1.8}$ behavior. If two photons are absorbed by the projectile, the cross section should display a Z_T dependence which is close to Z_T^4. If the one photon processes are competing with the two photon processes, the Z_T dependence would not be too steep but it would still be steeper than 1.8.

The analysis to test the existence of multi photon excitations consists of extracting the Z_T dependence (exponent) of the EMD cross sections for all the available decay channels. The exponent was extracted by fitting the formula given in the previous section to cross sections for Pb, Sn, Cu and Al targets. Since the formula contains 3 free parameters and we have only 4 targets (except for simple channels), the fit does not have sufficient constraints (only 1 degrees of freedom) to do a precision measurement. Table 6.4 shows the extracted parameters for 15 decay channels.

Figure 6.8 (a) shows the graphical representation of the extracted exponents against Q_0 for all the reaction channels. Due to poor statistics, the χ^2 minimization failed to converge for some of the channels, and hence were not included in the plot. No real enhancement was observed close to 40 MeV.

Table 6.4: Extracted exponents by a 3 parameter fit.

Channel	Q_0 (MeV)	a (mb)	b (mb)	c exponent
1p	11.6	(1.5±0.2) x10^{+0}	(2.0±0.3) x10^{-1}	1.84±0.03
1n	17.1	(8.6±1.3) x10^{-1}	(6.9±1.5) x10^{-2}	1.84±0.05
1p1n	24.7	(2.9±0.7) x10^{-1}	(1.7±0.8) x10^{-2}	1.87±0.12
2p	19.8	(1.9±0.4) x10^{-1}	(3.7±0.6) x10^{-2}	1.72±0.03
2p1n	30.9	(1.9±0.3) x10^{-1}	(0.9±0.3) x10^{-2}	1.75±0.07
2p2n	38.3	(0.5±0.2) x10^{-1}	(0.7±0.5) x10^{-2}	1.51±0.15
2n	30.5	(1.3±0.5) x10^{-2}	(0.1±0.1) x10^{-3}	2.15±0.25
2n1p	36.0	(3.3±1.1) x10^{-2}	(1.7±1.3) x10^{-3}	1.71±0.17
3p	34.0	(0.6±0.1) x10^{-2}	(0.6±1.3) x10^{-6}	3.11±0.52
3p1n	43.0	(1.4±0.3) x10^{-2}	(0.3±0.5) x10^{-4}	2.26±0.33
3p2n	49.9	(1.6±0.4) x10^{-2}	(2.8±2.9) x10^{-4}	1.88±0.24
4p	44.7	–	–	–
4p1n	53.6	(0.4±0.3) x10^{-3}	(0.3±1.4) x10^{-7}	2.91±1.08
4p2n	58.8	(2.0±1.0) x10^{-3}	(0.2±0.5) x10^{-4}	1.98±0.78
4p3n	69.1	–	–	–

A simple test enables us to measure the reliability of our fitting procedure in extracting the exponents. This is done by forcing the exponent to be 1.8 and repeating the exercise with 2 free parameters a and b. If we have enough sensitivity to extract the double photon excitation enhancement, and if our data truly support the idea, it should be reflected in the χ^2 probability distribution. It was found that both methods produce fairly flat distributions. This indicates that within our statistical accuracy, we cannot prove that the behavior of the data is other than $Z^{1.8}$.

Figure 6.8 (b) shows the ratio of the electromagnetic component to the soft nuclear component extracted by the 2 parameter fit for the decay channels. The ratio essentially gives us the contribution of the nuclear component to each peripheral channel. For higher Q values the nuclear component is large in comparison with the electromagnetic component. Unfortunately, this affects our fitting procedure since the nuclear component in the region $Q > 30$ is more than 25% of the total cross section.

3 Background to the Double Photon Excitation Process

A possible background to the double photon process could arise from the absorption of two single photons from two different target nuclei. A straightforward estimate can be made under the assumption that the cross sections for the removal of a few nucleons is roughly the same for the first and second interaction in the target material.

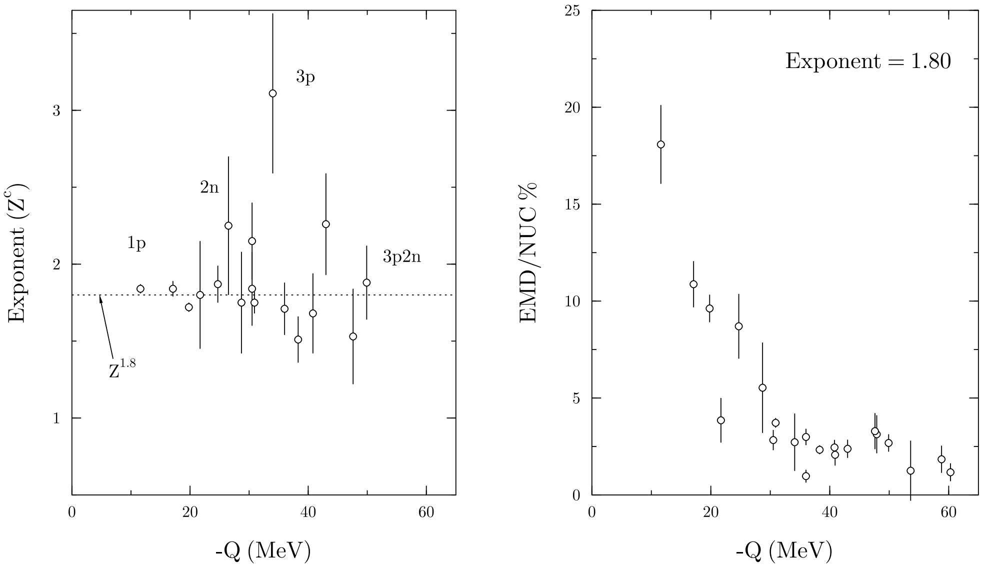

Figure 6.8: (a) Z dependence of cross sections extracted by the three parameter fit discussed in the text. (b) Ratio of nuclear and EMD components for different decay channels obtained with a fixed exponent.

For a target of thickness ℓ the flux of secondaries produced in a slice dx is given by:

$$dN = n\sigma N_0 dx$$

where, N_0 and σ are the original flux and the cross section respectively, for the first interaction. The constant n is the number density of the target nuclei.

The flux of produced particles after the second interaction in the target is given by:

$$dN' = n^2\sigma\sigma' N_0(\ell - x)dx$$

and the total yield is given by:

$$\frac{N'}{N_0} = \sigma\sigma' \frac{(n\ell)^2}{2}$$

If we generalize the above equation for multiple interactions, we would get;

$$\frac{N'}{N_0} = \left[\prod_{i=1}^{k} \sigma_i\right] \frac{(n\ell)^k}{k!}$$

where the σ_i's represent the cross sections for each interaction.

This formula allows us to evaluate the contribution of secondary interactions from two different nuclei, to the measured cross sections. Table 6.5 shows the percentage of the secondary interaction background of the measured cross sections for several decay channels. Out of all possible combinations, the most effective decay branches were considered. It is assumed here that even after the first interaction the residual nucleus will respond to the subsequent interactions in the same manner as the original projectile. The last two columns show the extracted exponents before and after the corrections due to the double interactions. It is clear from these results that the effects of the secondary interactions do enhance the exponent. Therefore, significant contributions of this type can produce enhancements which can be misidentified as the double photon absorption since they are target dependent.

Table 6.5: Estimated double scattering contribution on the cross sections. Here, c_{old} and c_{new} represents the old and new (after correcting the cross sections for the double scattering) exponents.

Channel	-Q (MeV)	Pb%	Sn%	Cu%	Al%	c_{old}	c_{new}
1p1n	24.7	3.2	1.6	0.9	0.3	1.87	1.84
2p	19.8	3.9	1.8	1.0	0.3	1.72	1.69
2p1n	30.9	3.4	1.7	0.8	0.3	1.75	1.73
2p2n	38.3	3.3	1.6	0.7	0.3	1.51	1.48
2n	30.5	19.3	11.0	6.4	2.1	2.15	1.99
2n1p	36.0	5.7	2.7	1.1	0.5	1.71	–
3p	34.0	111.9	96.0	43.7	9.9	3.11	–
3p1n	43.0	31.2	16.0	9.2	2.3	2.26	1.69

C Excitation Energy Reconstructions

To generate excitation energy distributions and decay angular distributions in θ^* and ϕ^*, events that were used in the evaluation of the cross sections of 1p and 1n were processed as described in the previous chapter. The experiment E814 is not designed to measure the energy of the emitting photon when the residual nucleii decay to an excited state before reaching the ground state. As a result, the true excitation energy cannot be measured. The effect of such decays on the measurement are discussed here. We concentrate on the 1p emission channel primarily, and occasionally, when needed, 1n results are discussed.

1 Single Nucleon Emission

1.1 Excitation Energy Distributions

In Figures 6.9 (a) and (b), the raw excitation energy distributions of selected events produced for 1p and 1n emission channels on Pb, Sn, Cu and Al targets are shown. Corrections for interactions outside the target have been done on these data. A

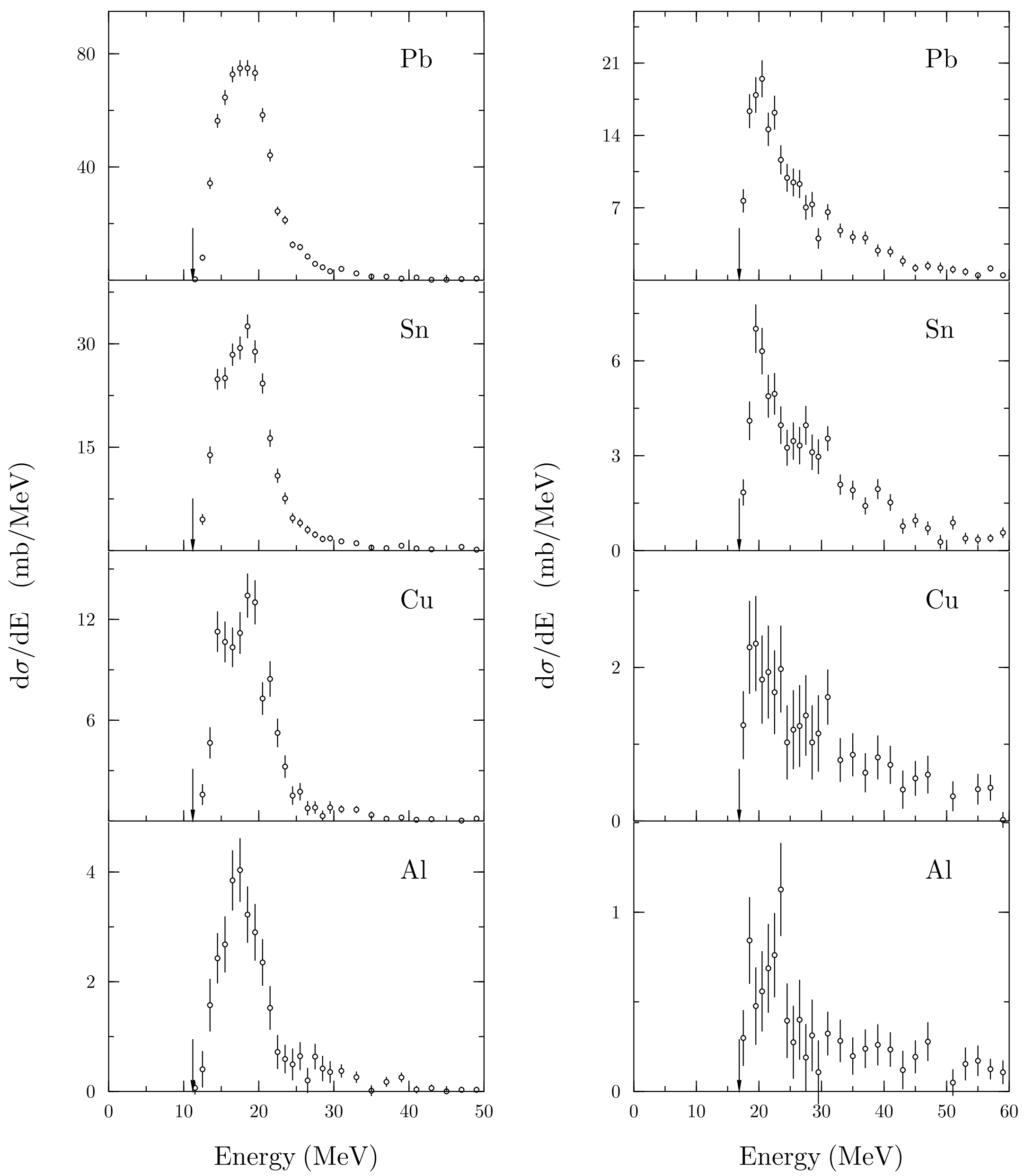

Figure 6.9: Reconstructed raw excitation energy spectra for 4 different targets. The arrows indicate the kinematic thresholds for each reaction. (a) 1p events. (b) 1n events.

correction of $\sim 5\%$ in Pb and $\sim 30\%$ in Al is obtained by the empty target subtraction. Our estimates of the experimental resolution in the invariant mass reconstruction discussed in chapter 5, section 3.2, is evident by the rapid rise of the data near the threshold.

A peak that is centered at about 18 MeV with a relatively narrow width of about 7 MeV is seen for all 1p distributions. These values can be compared with the values of peak position (20 MeV) and width (4.5 MeV) obtained for the GDR in ^{28}Si by the (γ,p) reactions [12, 13]. It should be noted that the virtual photon spectrum of the electromagnetic excitation process is not uniform and hence tends to enhance the low end of the GDR distribution. The decay to excited states in ^{27}Al produce a similar effect on these distributions.

For the 1n distributions the peak position and the width correspond to about 22 MeV and 5 MeV respectively. The available data obtained from the (γ,n) reactions [14] show a good agreement with our measurements. For 1n excitation, the threshold energy is already higher than the peak energy of the GDR and hence shows a sharp rise. The tail of the 1n distributions arises from events which are poorly reconstructed.

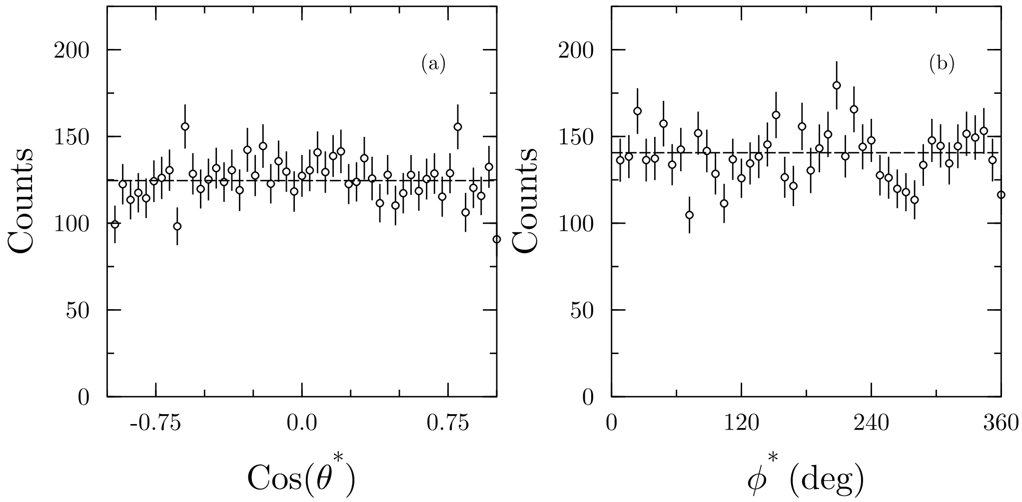

Figure 6.10: Decay angular distributions for reconstructed 1p events taken with a Pb target. The angles are the (a) polar (b) azimuthal center-of-mass angles of the ^{27}Al ion.

1.2 Angular Distributions

The polar (θ^*) and azimuthal (ϕ^*) center of mass angles of the ^{27}Al ions for the 1p emissions obtained from the kinematic reconstruction are presented in Figures 6.10 (a) and (b). Within statistics, both these distributions are very nearly isotropic (dashed lines) and symmetrical. This symmetry gives us confidence in the event reconstruction techniques used in this analysis. A detailed theoretical calculation of the expected shape of the decay angular distribution is complicated by the decays proceeding to the excited states of the residual nucleus. However, the preference for emission perpendicular to the beam axis, which is suggested by Bertulani and Baur [11] for spinless projectiles and fragments are not observed in our data.

Due to the poor resolution in the energy and position measurements in the calorimeters, we are unable to extract the center of mass angles for the 1n distributions.

1.3 Ratios of Energy Spectra

By assuming that the process is factorizable, i.e. that the differential cross section is proportional to $N_\gamma \cdot \sigma(\gamma, p)$ where N_γ is related to the excitation mechanism, insight into the dependence of the reaction mechanism on the excitation energy, can be gained by using the ratios of the energy spectra for different targets. For example, if the excitation is purely nuclear, the obtained ratio should be proportional to the sum of the target and the projectile radii, whereas a purely electromagnetic excitation should give a ratio that scales with the target charge as a power of Z_T. For high Z targets, the ratios should be equal to the ratios of the calculated photon spectra since soft nuclear background makes a non negligible contribution.

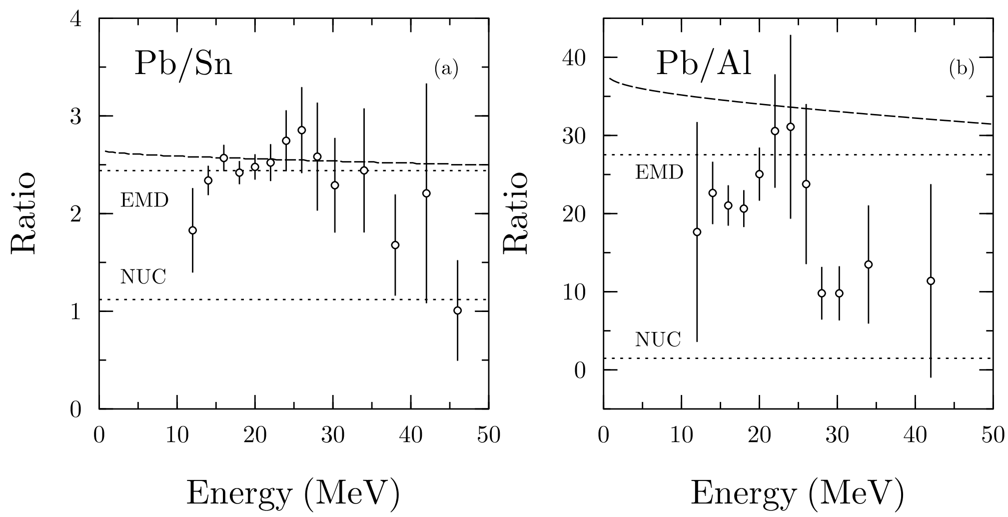

Figure 6.11: Ratio of excitation energy spectra for (a) Pb/Sn and (b) Pb/Al. Two dotted lines indicate the expected ratios for pure nuclear and pure electromagnetic dependence. Dashed lines represent the theoretical ratio obtained by the WW method.

The experimental ratios for Pb/Sn and Pb/Al compared with the ratios expected from the two terms EMD and nuclear (dotted lines) are shown in Figures 6.11 (a) and (b). The two terms are extracted from the fit performed on the integrated 1p cross sections which was discussed earlier. In addition, the ratios of the calculated photon spectra (dashed lines) for the same targets are shown in the figure. It is assumed in the calculation of the photon spectra that the minimum impact parameter b_{min} is the sum of the target and the projectile radii:

$$b_{min} = 1.2(A_T^{1/3} + A_P^{1/3}).$$

The ratios near the GDR for the Pb/Sn are fairly consistent with the calculated ratio. This is not true for the Pb/Al targets. The experimental ratios obtained for the Pb/Al targets are much lower than the calculated values. At the high end of the energy spectrum (E > 25 MeV), the nuclear background is clearly the dominant process. The data also indicate some background at low excitation energies. Although the ratios of the calculated WW spectrum are consistently higher than the data, at least in the vicinity of the GDR, the ratio of the photon spectra agrees quite well with the data.

A similar behaviour was observed with the 1n data. An enhancement indicating the presence of DGDR in the experimental data for Pb/Al close to an excitation energy of 40 MeV was not observed in both the 1p and the 1n distributions.

1.4 Nuclear Background Subtraction

A technique similar to that used for the integrated cross sections was used to evaluate the contribution of the nuclear background as a function of the excitation energy. This is required since the decay channels originating from nuclear induced interactions and electromagnetic interactions cannot be distinguished on an event by event basis. To initiate this technique, an approximate experimental distribution for the nuclear component was obtained by assuming that the data from the Pb target has a negligible nuclear background (it was shown earlier that the Pb target nuclear contamination is only 2%). This method is applied on the 1p data.

The data in Figure 6.9 (a) were first rebinned into energy bins of width 2-4 MeV (see Table 6.6) to obtain sufficient statistical accuracy. The Pb data were then scaled by the factor $(Z_C/Z_{Pb})^{1.8}$ and subtracted from the data taken with the Carbon target (the excitation energy distribution for the C target is not shown in Figure 6.9). This produced the expected distribution of the nuclear induced component for the C target. This is is shown in Figure 6.12. It was found that a sum of a Gaussian and a Moyal function [2], each with three free parameters, fits this extracted distribution quite well. The function used is

$$f_{NUC} = X_1 e^{-\mu^2/2} + X_2 e^{-(\lambda + e^{-\lambda})/2}$$

in which $\mu = (E - X_3)/X_4$ and $\lambda = (E - X_5)/X_6$.

The procedure is to perform a fit of the following function to the entire data set:

$$d\sigma_k/dE = (A_T^{1/3} + A_P^{1/3}) f_{NUC} + Z^{1.8} C_k(E_k)$$

[2]The selection of these two functions does not have any scientific basis.

in which the 6 nuclear parameters (X_i) and 14 values of C_k (one for each value of the excitation energy E_k) are varied to minimize the χ^2 of the fit.

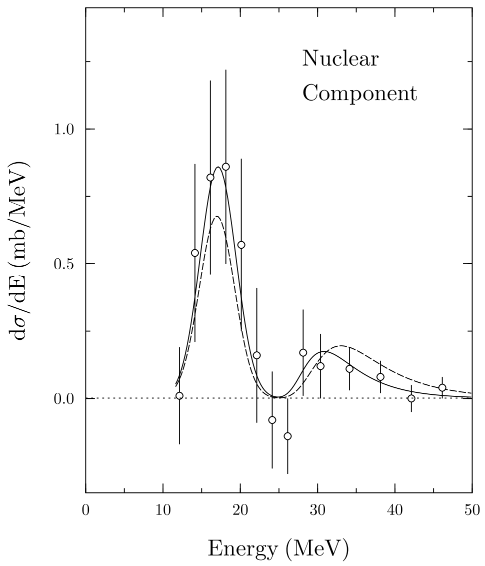

Figure 6.12: Estimated cross section distribution of the surviving nuclear induced component of the cross section for the C target, obtained by subtracting the raw Pb data, scaled by a factor $(Z_C/Z_{Pb})^{1.8}$, from the C data.

To test the method of separating the two components, a fit was performed on the data from the four targets Pb, Sn, Cu, and Al. These results were used to predict the nuclear component of the C data. To obtain sufficient accuracy in this test, it was necessary to represent C_k as a parametrized function. The same form used to represent f_{NUC}, was used to represents C_k in this test. The fit obtained for the above mentioned four targets, is given by the dashed curve in Figure 6.12. No data from the C target was used here. It is clear that the function f_{NUC} found in this fit is consistent with the nuclear component of the C data. This demonstrates the validity of the method. To achieve an optimal accuracy for this subtraction, the C data were included in the final fit. The solid line in Figure 6.12 represents the resulting nuclear component extracted from this fit. The χ^2 for this fit is 31.6 for 50 degrees of freedom. The fitted nuclear component from each of the data points of Figure 6.9 (a) were then subtracted to obtain the experimental EMD cross sections for each target.

Figure 6.13 gives the background-subtracted EMD final energy spectra for the Pb, Sn, Cu and Al targets. The effects of the nuclear excitation were as expected negligible for the heavier targets. The main effect for the Al target was the reduction of the cross section at the peak by approximately 20%, and the reduction of the high energy tail which was quite significant. The EMD component resulting from the fit is given in Table 6.6. Values of the nuclear component are also obtained from this fit, but since the trigger and the event selection procedure have already been applied to remove events of this nature, these cannot be considered as meaningful measurements for nuclear component.

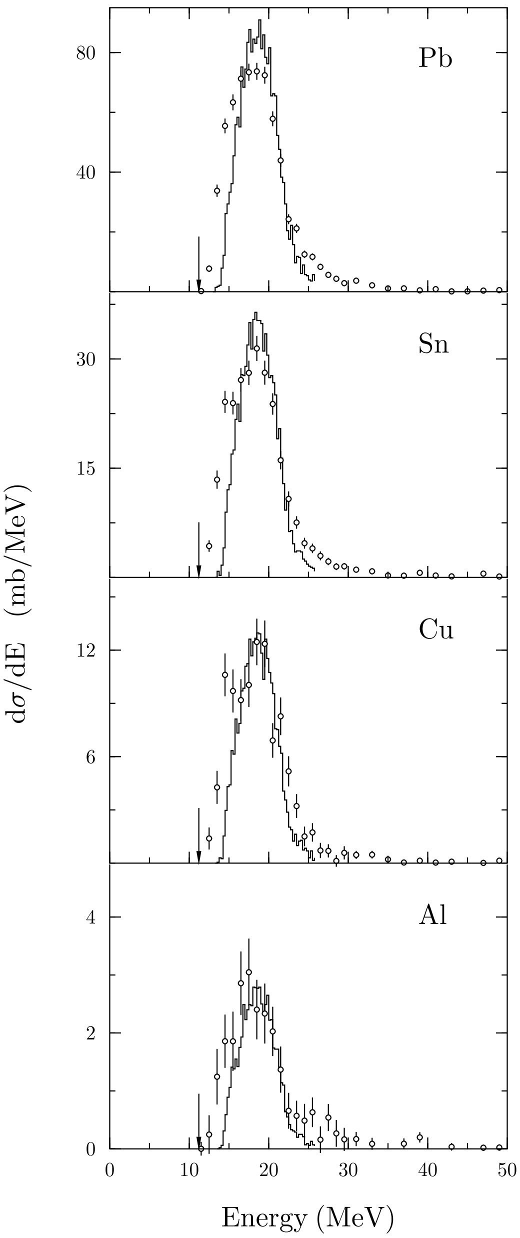

Figure 6.13: Nuclear component subtracted excitation energy spectra for reconstructed 1p events taken with 4 targets. The solid curves are obtained from (γ, p) experimental data multiplied by the WW spectrum and simulated through our apparatus. The arrows indicate the kinematic threshold of the reaction.

Table 6.6: Values of the cross section parameters C_k found in the final fit to the data taken with Pb, Sn, Cu, Al and C targets.

E_k(MeV)	C_k(μb/MeV)	E_k(MeV)	C_k(μb/MeV)
11-13	1.54 $\pm$ 0.20	25-27	3.36 $\pm$ 0.23
13-15	16.22 $\pm$ 0.51	27-29	1.69 $\pm$ 0.18
15-17	23.42 $\pm$ 0.61	29-32	1.16 $\pm$ 0.13
17-19	26.28 $\pm$ 0.64	32-36	0.56 $\pm$ 0.08
19-21	23.09 $\pm$ 0.58	36-40	0.31 $\pm$ 0.06
21-23	12.26 $\pm$ 0.40	40-44	0.18 $\pm$ 0.05
23-25	5.77 $\pm$ 0.29	44-48	0.09 $\pm$ 0.03

2 Comparison with Low Energy Data

2.1 Partial Cross Sections

Comparison of the results of this experiment with data from the photo-nuclear process is required to understand the properties of the virtual photon field. For this comparison, available data on the ^{28}Si(γ,p)^{27}Al reactions [12, 13] can be used. To predict the results expected in our experiment, the WW spectrum was combined with the photo-nuclear cross section measurements using a simulation program. For 1p distributions, this program uses experimental (γ,p) cross sections for ^{28}Si measured up to an energy of $E_\gamma = 26.0$ MeV. It takes into account the decay to excited states of ^{27}Al of energy up to 4.5 MeV [12]. The prediction is done as follows.

For each state in ^{27}Al, the (γ,p) differential cross sections are first multiplied with the virtual photon spectrum. This provides the effective final state yields as functions of the photon energy. These yields are then integrated over the photon energy and the resulting values are used to obtain effective branching ratios for each state. The excited state based on these ratios is selected, and a value for the photon energy is generated according to the strength distribution of the state being considered. The decay is assumed to be isotropic. As mentioned before, in the case of decay to an excited state of ^{27}Al, the energy of the proton is reduced, which results in the enhancing of the lower end of the observed excitation energy distribution. The simulation includes the effects of detector resolution and multiple scattering.

Although the invariant mass (which is the excitation energy of the p+^{27}Al system) is measured, the real excitation energy is the sum of the measured energy and the energy of any undetected decay photons from the ^{27}Al nucleus. It is possible to study the relationship between the two by using the simulation code. The expected excitation energy distribution for the calculation described above is shown in Figure 6.14. The sum of the energy of the decay photon and the excitation energy is also shown for comparison. The systematic uncertainty made in interpreting the measured energy as the excitation energy can be estimated by the difference between the two curves. Only excited states of ^{27}Al of 4.5 MeV or lower are included in this simulation (since they are the only available states which we could find in the literature). The difference between the measured excitation energy and the true excitation energy will be affected by the existence of higher excited states, but for excitation energy values below 20 MeV in ^{28}Si, due to the Q value of the reaction, it is unlikely that states of energy above 4.5 MeV will be excited.

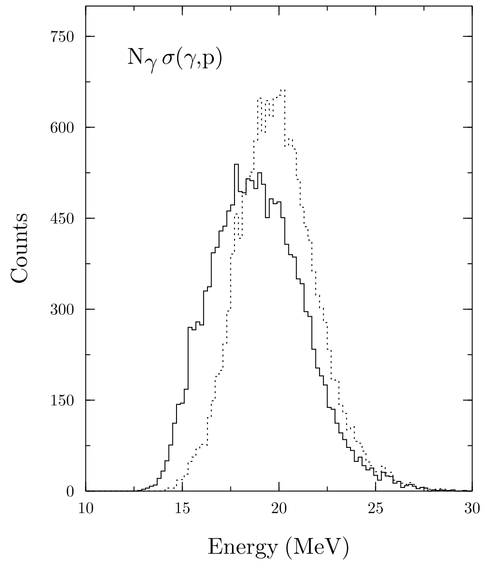

Figure 6.14: Monte Carlo simulation of the measured excitation energy distribution (solid curve) and the true excitation energy distribution (dashed curve), obtained by adding the energy of the decay photon to the measured energy. The calculation is for Pb target.

For comparison, the excitation energy curves obtained from the Monte Carlo simulation are displayed with the data in Figure 6.13. There are no adjustable parameters in this comparison. A comparison beyond 26.0 MeV cannot be made since the simulation, which uses the $\sigma(\gamma, p)$ cross section data are available only in the interval 15.4 - 26.0 MeV. The value obtained by integrating the simulated cross sections over the excitation energy in the interval 16.0-26.0 MeV agrees well with the data. They are shown in Table 6.7.

However, a small discrepancy in shape is observed at the low end of the excitation energy spectrums. By simulating the events using different detector alignments and resolutions, an attempt was made to understand whether this discrepancy was due to instrumental effects. Noticeable differences in the decay angular distributions were produced, but the excitation energy spectrum was insensitive to these changes. The observed discrepancy could be an indication of the inability to explain the excitation of the resonance with a simple WW approximation or, the effect of excited states of ^{27}Al above 4.5 MeV, as mentioned above.

A similar comparison was made between the reconstructed 1n results and the ^{28}Si$(\gamma,n)^{27}$Si data obtained from the reference [14]. Figure 6.15 shows the comparison

Table 6.7: Integrated cross sections in the interval 16.0 to 26.0 MeV. The errors for the simulation are deduced from the available $^{28}Si(\gamma,p)^{27}Al$ photo-absoption cross sections which are used as the input. Errors on the data are statistical.

Target	Data (mb)	Simulation (mb)
Al	20.3 ± 1.6	15 ± 4
Cu	91.4 ± 3.7	72 ± 20
Sn	230.0 ± 4.9	203 ± 55
Pb	581.2 ± 8.3	515 ± 141

for the Pb target. No attempt was made to subtract the nuclear component from the 1n data since it has very little affect on the Pb target (only 2% nuclear contamination). The agreement between our results and the low energy data is satisfactory, showing a similar excess at the upper end of the curve as it seen for the 1p data. The tail out to higher energies (> 40 MeV) is a result of poor reconstruction for 1n events.

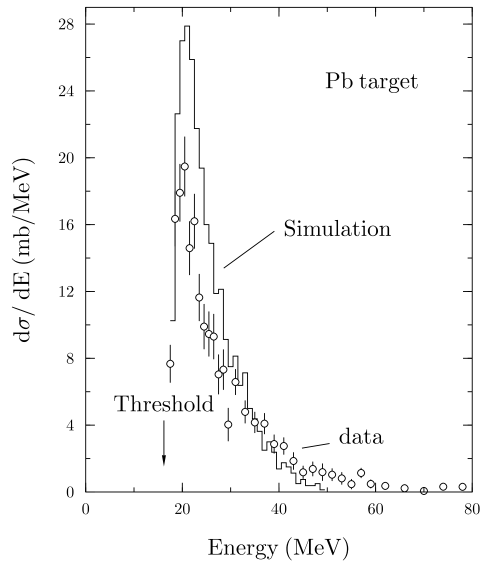

Figure 6.15: Excitation energy for 1n decay (closed circles). The solid curve represents the (γ, n) multiplied by the WW spectrum and convoluted with our experimental resolution. Arrows indicate the kinematic thresholds.

2.2 Verifications of the Total Cross Section Scale

The fragmentation of ^{28}Si at 14.6 GeV/nucleon was previously measured by using plastic nuclear track detectors [23]. These measurements report a total charge changing cross section value of 1190±170 mb since they measured $\Delta Z \geq 1$, missing the 1n cross section. If we correct for this effect, the total EMD cross section will be

1430±180 mb. The integrated EMD from Weizsäcker Williams is 1500 mb which is in very good agreement with the measured data.

From the beam trigger tapes, we measure 1410±100 as the total EMD cross section. This number is an upper limit on all the cross sections we can obtain. The error is quite large due to the poor statistics in the beam trigger tapes. If we add together the cross sections given in Tables 6.2 and 6.3, we obtain about 1250 mb, in agreement with the expected value. The cross section measured for 1p, 1n and 2p channels result in about 1000 mb which is about 70% of the total cross sections. Since we can reconstruct 1p, 1n and 2p channels, we can use the sum of these to compare with the total cross sections measured. Reconstruction of the 2p channel is not part of this thesis, but a precision measurement of this process has been carried out within the collaboration. We use these results only for the present cross section discussion.

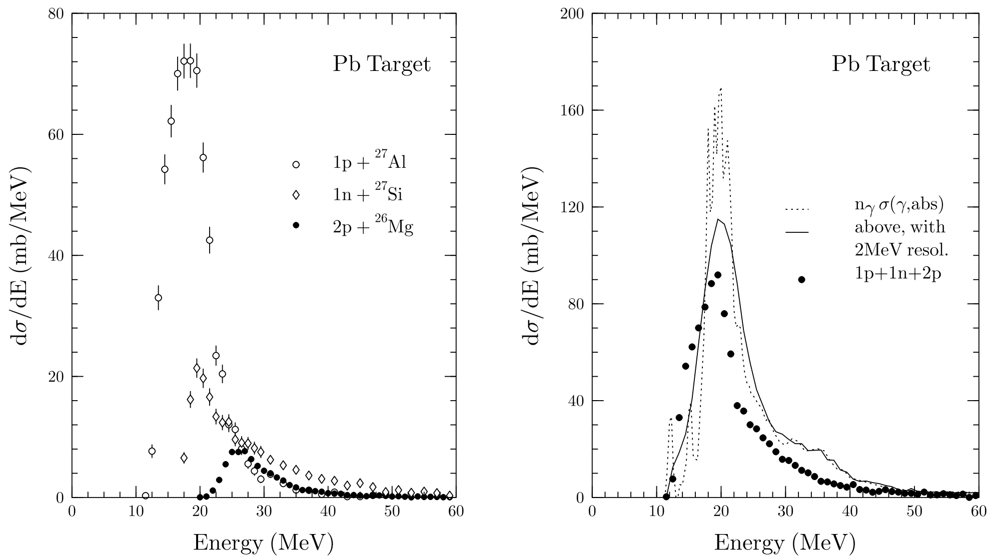

Figure 6.16: (a) Excitation energy distributions of 1p, 1n and 2p decay. (b) Sum of the three distributions compared with (γ,abs) spectra.

Figure 6.16 (a) shows the measured 1p, 1n and 2p excitation energy distributions for the Pb target. Although the distributions rise at different locations due to different thresholds, they agree remarkably well at the trailing edge of the GDR. Figure 6.16 (b) shows the measured total absorption cross section compared with our reconstructed sum of 1p, 1n and 2p distributions. The total absorption cross section curve is convoluted with our resolution. Although we measure only 70% of the total cross section by these three channels, the agreement is quite good.

CHAPTER 7

Conclusions

This work presents the results of an experimental investigation of the electromagnetic dissociation of 14.6 GeV/nucleon ^{28}Si ions. Exclusive cross section measurements for a large number of decay channels and excitation energy reconstruction for two simple decay channels having a single proton and a single neutron in the final state are studied. The reconstruction methods and techniques developed here can be extended to more complex channels quite easily.

In the past, the electromagnetic component was obtained by subtracting the hadronic contribution from the integrated total cross sections, using estimated values based on the concept of limiting fragmentation. Recent experiments, including experiment E814, have used the information from the production of secondary particles to reject the hadronic background electronically. It has been shown here that such techniques are very useful in suppressing the nuclear background and enabling the study of complex electromagnetic dissociation decay channels.

The measured cross sections presented here are in good agreement with those measured previously [31] with the E814 apparatus. Because the two experimental setups differ considerably, particularly in the detectors used to veto nuclear events, the agreement of the two results indicates that the event selection procedure and efficiency estimates are reliable. The observed dependence of the measured cross sections on the target charge Z_T and target mass A_T indicate the electromagnetic nature of the excitation mechanism. The measured cross section ratio $\sigma(\gamma,\mathrm{p})/\sigma(\gamma,\mathrm{n})$ is 2.7$\pm$0.7 for E$_\gamma$ up to 30 MeV [14]. We observe a ratio of 2.81$\pm$0.21 for the Pb target and 2.41$\pm$0.18 for the Al target indicating a excitation of GDR in ^{28}Si. The measured semi-inclusive cross sections agree well with the previously measured charge changing cross sections [23]. These measurements were obtained by detecting only the heavy fragment and hence set an upper limit to our data. All cross sections show an approximate $Z_T^{1.8}$ behavior which is well reproduced by the WW approximation. The contribution due to the hadronic processes tends to increase for decay channels with higher Q values.

The excitation energy distributions of the decay channels $^{28}\mathrm{Si} \rightarrow 1\mathrm{p}+{}^{27}\mathrm{Al}$ and $^{28}\mathrm{Si} \rightarrow 1\mathrm{n}+{}^{27}\mathrm{Si}$ were reconstructed with geometrically and kinematically constrained fits. With the E814 apparatus, the former was reconstructed with 3 geometrical constraints and 2 kinematical constraints whereas the latter was reconstructed with 1 geometrical constraint and 1 kinematical constraint (neglecting the energy measurement). Results show that the reconstruction techniques provide a resolution of 0.6-1.1 MeV (depending on the target) for 1p events and ≈ 2.0 MeV for 1n events (at ~ 20 MeV of excitation energy) in the invariant mass reconstruction. Center of mass angles for 1p decay were reconstructed to an accuracy of a few degrees. The resolution in both energy and angle is dominated by multiple scattering in the target. Poor resolution in the energy measurement in the calorimeters prevents the reconstruction of angular distributions for 1n decay with good precision.

The soft nuclear-induced background to the EMD in the final state energy distributions for 1p decay was evaluated by representing this component with a simple functional form, whose parameters were determined by a fit to the data for all targets. The effect of the nuclear contribution was negligible for high Z targets, but was substantial for low Z targets. However, the parameters obtained for the nuclear component cannot be taken as meaningful measurements of the nuclear component of the cross section since the trigger and the selection procedure introduce severe biases to this process. The resulting EMD spectrum was compared with the results of a simulation based on a folding of the WW virtual photon spectrum produced by the targets with the inverse photonuclear process ^{28}Si(γ,p)^{27}Al. In general, the agreement is satisfactory, but some discrepancy is observed at low final state energies. A similar effect has been seen in the data on the EMD of ^{16}O at lower beam energies [22]. The same technique can be used to subtract the nuclear-induced background in the 1n excitation energy distributions.

A possibility for two photon excitations in EMD was investigated with a simple parametrization given by equation 6.1. The theoretical calculations suggest that the ratio of single photon excitation to double photon excitation in ^{28}Si at 14.6 GeV/nucleon is extremely small. In addition, successive one photon excitations for two different target nuclei can induce the same signatures as 'real' double photon excitations for a single nuclei. It has been shown that for some decay channels (for example the 3p emission channel) this makes a substantial contribution to the integrated cross section. The extracted parameters indicate that our data provide no evidence for the DGDR excitations in ^{28}Si. The ratios of excitation energy distributions for ^{208}Pb/^{27}Al and ^{208}Pb/^{120}Sn show a similar behavior. The ratios agree quite well with the expected behavior of the WW approximation. However, Q values above 30 MeV ratios show large deviations from the expected WW calculations which indicates that nuclear processes are substantial in this region. This in itself makes observations of DGDR very difficult through a total cross section measurement since the hadronic contribution becomes large in the region where we expect to observe signatures of DGDR.

There are obvious shortcomings in our experiment. We have a substantial inefficiency in detecting particles emitted at angles between 45^o and 180^o which are covered by the target calorimeter. The estimated leakage of this detector is roughly 50%. Efficiency in U/Cu calorimeters are not very good, especially in the region where the neutrons are detected (about 90%). This is caused by having two calorimeter modules aligned at the center of the neutron distribution. This makes it extremely difficult to obtain clean samples of events for the reconstruction, in all exclusive EMD decay channels. Poor resolution in the U/Cu calorimeter energy and position measurements too do not allow us to reconstruct neutron channels with good precision. Studies have shown that by reconstructing residual heavy ions to a much higher degree than what is achieved in this thesis, this problem can be eliminated up to some extent. We cannot detect the de-excited γ rays emitted by the excited nucleus which can have a tremendous effect on observing DGDR excitations. In addition, multiple scattering in the target medium contributes substantially to the final reconstruction resolution. This can be easily avoided by using thin targets which would in addition reduce the contribution due to the double interaction background.

In spite of these short comings, the present work has shown that at relativistic energies it is possible to measure the properties of excited heavy ion projectiles with a resolution that is good enough to probe their structure. Other nucleii and decay channels can be studied using the techniques given here. For example, the collective states in the continum of unstable nuclei, and the existence of collective strength at high excitation energies which are above the GDR can be explored using these techniques. In addition, by using the precision kinematic reconstruction of exclusive channels, it is possible to study the correlation of final states containing identical particles.

REFERENCES

[1] D.L. Olson at el., "Electromagnetic Dissociation of Relativistic ^{18}O Nuclei" *Phys. Rev. C* 24, 1529 (1981).

[2] M.T. Mercier et al., "Electromagnetic Dissociation of ^{59}Co, ^{89}Y and ^{197}Au Targets by Relativistic Heavy Ions to Z = 26" *Phys. Rev. C* 33, 1655 (1986).

[3] J.C. Hill et al., Electromagnetic Dissociation of ^{39}Co and ^{197}Au Targets by Relativistic ^{139}La Projectiles" *Phys. Rev. C* 38, 1722 (1988).

[4] J.C. Hill et al., "Two-Neutron Emission from Electromagnetic Dissociation of ^{59}Co and ^{197}Au Targets by Relativistic Heavy Ions" *Phys. Rev. C* 39, 524 (1989).

[5] T. Kobayashi et al., "Electromagnetic Dissociation and Soft Giant Dipole Resonance of the Neutron-Dripline Nucleus ^{11}Li" *Phys. Lett B* 232, 51 (1989).

[6] H. Takai, "Electromagnetic Dissociation and Projectile Fragmentation of Relativistic heavy Ions" *International Jour. Modern Phys.* (to be published).

[7] K. Goulianos, "Diffractive Interactions of Hadrons at High Energies" *Phys. Rep.* 101, 169 (1983).

[8] W.E. Frahn, "Diffraction Scattering of Charged Particles" *Anna. Phys.* 72, 524 (1972).

[9] H.R. Blieden, Measurement of Small-Angle Elastic Scattering of Pions and Protons by Nuclei" *Phys. Rev. D* 11, 14 (1975).

[10] J.D. Jackson, "Classical Electrodynamics", *Wiley* (1974).

[11] C.A. Bertulani and G. Baur, "Electromagnetic Processes in Relativistic Heavy Ion Collisions", *Phys. Rep.* 163, 299 (1988).

[12] R.L. Gulbranson et al., "Charged Particle Decay of the ^{28}Si Giant Electric Dipole Resonance" *Phys. Rev. C* 27, 470 (1983).

[13] E. Kerkhove et al., "Charged Particle Decay of ^{28}Si Induced by Quasi-Monochromatic Annihilation Photons in the GDR" *Nucl. Phys.* A474, 397 (1987).

[14] R.E. Pywell et al., "Photoneutron Cross Sections for the Silicon Isotopes" *Phys. Rev. C* 27, 960 (1983).

[15] C.J. Benesh et al., "Single Nucleon Removel in Relativistic Nuclear Collisions" *Phys. Rev C* 40, 1198 (1989).

[16] J.W. Norbury, "Charge Dependence and Electric Quadrupole Effects on Single-Nucleon Removal in Relativistic and Intermediate Nuclear Collisions" *Phys. Rev C* 42, 2259 (1990).

[17] J.W. Norbury, Electric Quadrupole Excitations in Relativistic Nucleus-Nucleus Collisions" *Phys. Rev C* 42, 711 (1990).

[18] D. Lissauer and H. Takai, "Z Dependence of Coulomb Dissociation Cross Section in Heavy Ion Reactions" *Phys. Rev. C* 41, 2410 (1990).

[19] W.J. Llope and P. Braun-Munzinger, "Electromagnetic Dissociation of Relativistic Heavy Ions" *Phys. Rev. C* 41, 2644 (1990).

[20] W.J. Llope, "The Dissociation of Relativistic Nuclei", *Ph.D. Thesis*, SUNY at Stony Brook, (1992).

[21] R. Schmidt et al., "Double Giant Dipole Resonance in ^{136}Xe" *Phys. Rev. Lett* (Submitted).

[22] D.L. Olson et al., "Direct Observation of the Giant Dipole Resonance of ^{16}O via Electromagnetic Dissociation" *Phys. Rev. C* 44, 1862 (1991).

[23] C. Brechtmann et al., "Fragmentation Cross Sections of ^{28}Si at 14.6 GeV/nucleon" *Phys. Rev. C* 39, 2222 (1989).

[24] J. Stachel and G. Young, "Relativistic Heavy Ion Physics at CERN and BNL" *Anal. Rev. Nucl. Part. Sci.* 42, 237 (1992).

[25] P. Braun-Munzinger et al., "Study of Extremely Peripheral Collisions and of the Transition from Peripheral to Central Collisions in Reactions Induced by Relativistic Heavy Ions", *E814 proposal submitted to the AGS committee* 56 (1985).

[26] J. Sandweiss et al., "Search for Strange Matter and Antinuclei in E814", *E814 proposal submitted to the GAS committee* (1988).

[27] P. Braun-Munzinger et al., "Transverse Energy Distrubutions in Si-nucleus Collisions at 10GeV/nucleon", *Z. Phys. C* 38, 45 (1988).

[28] J. Barrette et al., "Energy Flow and Stopping in Relativistic Heavy-Ion Collisions at $E_{lab}/A = 14.6$ GeV", *Phys. Rev. Lett.* 64, 1219 (1990).

[29] J. Barrette et al., “Forward Baryons in Relativistic Nucleus-nucleus Collisions”, *Phys. Rev. C* 45, 819 (1992).

[30] J. Barrette et al., “Charged Particle Multiplicity in ^{28}Si+Al, Cu and Pb Rections at $E_{lab}/A = 14.6$ GeV”, *Phys. Rev. C* 46, 312 (1992).

[31] J. Barrette, et al., “Electromagnetic Dissociation of ^{28}Si at $E_{lab}/A = 14.6$ GeV by Nucleon Emission”, *Phys. Rev. C* 41, 1512 (1990).

[32] J. Barrette et al., “Electromagnetic Dissociation of Relativistic ^{28}Si into p+^{27}Al”, *Phys. Rev. C* 45, 2427 (1992).

[33] J. Barrette et al., “Production of Neutron-rich Isotopes from the Fragmentation of ^{28}Si Projectiles at $P_{lab} = 14.6$ GeV/c per nucleon”, *Phys. Rev. C* (to be published).

[34] F.S. Rotondo, “Limits on Strange Quark Matter Production” Ph.D. Thesis Yale University (1991).

[35] J. Barrette et al., “Search for Strange Quark Matter in High Energy Heavy Ion Collisions”, *Phys. Lett. B* 252, 550 (1990).

[36] J. Barrette et al., “Antiproton Production in Relativistic Si-Nucleus Collisions”, *Phys. Rev. C* (to be published).

[37] H. Takai and W.E. Cleland, “Trigger Processor for Experiment 814”, *E814 note* 32 (1988).

[38] R.M. Sternheimer, “Methods of Experimental Physics”, *Academic Press* Vol. 4A (1961).

[39] P.V. Vavilov, “Ionization Losses of High-Energy Heavy Particles”, *Sovi. Phys. JETP* 5, 749 (1957).

[40] G.D. Badhwar, “Calculation of the Vavilov Distribution Allowing for Electron Escape from the Absorber”, *Nucl. Inst. Meth.* 109, 119 (1973).

[41] J.H. Adams et al., “Calculation of the Vavilov Distribution”, *Nucl. Inst. Meth.* 124, 551 (1975).

[42] T. Akesson et al., “Properties of a Fine-Sampling Uranium-Copper Scintillator Hadron Calorimeter”, *Nucl. Inst. Meth.*, A241, 17 (1985).

[43] T. Akesson et al., “Performance of the Uranium/Plastic Scintillator Calorimeter for the HELIOS Experiment at CERN”, *Nucl. Inst. Meth.*, A262, 243 (1987).

[44] M. Fatyga et al., “Fast Monte Carlo Simulation of Segmented U/Cu/Scint Calorimeter”, *Nucl. Inst. Meth.*, A284, 323 (1989).

[45] R. Debbe et al., "A Study of Wire Chambers with Highly Segmented Cathode Pad Readout for High Multiplicity, Charged Particle Detection", *IEEE Trans. Nucl. Sci.*, NS-37, (1990).

[46] J. Fischer et al., "A Many Particle-Tracking Detector with Drift Planes and Segmented Cathode Readout", *IEEE Trans. Nucl. Sci.*, NS-37 (1990).

[47] M.H. Salamon et al., "Plastic Scintillator response to Relativistic Ne, Ar, Fe Ions" *Nucl. Inst. Meth.* 195, 557 (1982).

[48] R. Dwyer et al., "Plastic Scintillator response to Relativistic Nuclei Z$\leq$28" *Nucl. Inst. Meth.*, A242, 171(1985).

[49] J.B. Birks, "The Theory and Practice of Scintillation counting" *Macmillan*, NY, (1964).

[50] T. Tanimori et al., "A test of 150x20cm^2 wide time of flight scintillation counters" *Nuc. Inst. Meth.*, 216, 57(1983).

[51] T. Sugitate et al., "100cm long time of flight scintillation counters with rms resolution 50ps" *Nuc. Inst. Meth.*, A249, 354(1986).

[52] R. Wigmans et al., "On the Energy Resolution of Uranium and other Hadron Calorimeters" *Preprint Number* CERN/EP 86-141 (1986).

[53] J.P. Dishaw, "The Production of Neutrinos and Neutrinos-like Particles in Proton-Nucleus Interactions" *SLAC Report*, 216, March (1979).

[54] T. Ferbel, "Experimental Techniques in High Energy Physics" *Addison-Wesley Publishing Co.* (1987).

[55] B. Yu, "Gas Proportional Detectors with Interpolating Cathode Pad Readout for High Track Multiplicities" *Ph.D. Thesis*, University of Pittsburgh (1991).

[56] H. Wind, "In Formulae and Methods in Experimental Data Evaluation" *European Phys. Soci.* Vol 3, Chap k (1984).

[57] G. Conforto et al., "A Measurement of the β-parameter in the Charged Nonleptonic of the Λ^o Hyperon" *Nucl. Phys.* B40, 221 (1972).

[58] J.J. Russell et al., "Observation of Muon Trident in Lead and the Statistics of the Muon" *Phys. Rev. Lett.* 26, 46 (1971).

[59] E. Arik et al., "Y^* Production in Σ-Nucleus Reactions" *Phys. Rev. Lett.* 38, 1000 (1977).

[60] W.E. Cooper et al., "Studies in the BNL Negative 21 GeV/c Hyperon Beam I: Σ and Ξ Production Asymmetry in the Decay $\Xi^- \to \Lambda\pi^-$" *Phys. Rev. D* 21, 12 (1980).

[61] A.H. Wapstra and K. Bos, "Atomic Data and Nuclear Data Tables" Vol 19, 177 (1977).

[62] G. Lutz, "Optimum Track Fitting in the Presence of Multiple Scattering" *Nucl. Inst. Phys. Res.* A273, 349 (1988).

[63] G. Baur, "Multiple Electromagnetic Dissociation with Relativistic Heavy Ions" *Z. Phys. A* 332, 203 (1989).

[64] G. Baur and N. Baron, "Studies on Multiple Electromagnetic Excitation with Fast Heavy Ions: Scaling Properties for the Excitation of Rotational-Vibrational States" *J. Phys. G* 15, 661 (1989).

[65] L. Gonzaga et al., Covariant Formulation of Coulomb Excitation in Heavy Ion Collisions at Untra-Relativistic Energies" *Nucl. Phys.* A499, 837 (1989).

[66] D. Galetti et al., "A QED Description of Relativistic Coulomb Excitation in Heavy Ion Collisions" *Anna. Phys.* 177, 229 (1987).

[67] L.W. Townsend et al., "Calculations of Hadronic Dissociation of ^{28}Si Projectile at 14.6A GeV by Nucleon Emission" *Phys. Rev. C* 43, R2045 (1991).

[68] C. Brechtmann and W. Heinrich, "Fragmentation Cross Sections of ^{32}S at 0.7, 1.2 and 200 GeV/nucleon" *Z. Phys. A* 331, 463 (1988).

[69] C. Brechtmann and W. Heinrich, "Fragmentation Cross Sections of ^{16}O at 60 and 200 GeV/nucleon" *Z. Phys. A* 330, 407 (1988).